Ultra-low velocity zone beneath the Atlantic near St. Helena

Felix Davison [1], Carl Martin [1,2], Rita Parai [3], Sanne Cottaar [1]

[1]Department of Earth Sciences, University of Cambridge
[2]Faculty of Geosciences, Utrecht University
[3]Department of Earth, Environmental, and Planetary Sciences, Washington University in St. Louis

Key Points:

- Observation of significant S_{diff} postcursors sampling the CMB beneath the Atlantic
- Modelling of postcursors reveals a previously unknown mega-ULVZ situated on the CMB to the West of St. Helena
- Further measurements of St Helena and Ascension samples are needed to identify a potential ULVZ-associated geochemical signature

Corresponding author: Felix Davison, fpd21@cam.ac.uk

Abstract

There are various hotspots in the Atlantic ocean, which are underlain by mantle plumes that likely cross the mantle and originate at the core-mantle boundary. We use teleseismic core-diffracted shear waves to look for an Ultra-Low Velocity Zone (ULVZ) at the potential base of central Atlantic mantle plumes. Our data set shows delayed postcursory phases after the core-diffracted shear waves. The observed patterns are consistent in frequency dependence, delay time, and scatter pattern with those caused by mega-ULVZs previously modelled elsewhere. Synthetic modelling of a cylindrical structure on the core-mantle boundary below St. Helena provides a good fit to the data. The preferred model is 600 km across and 20 km high, centred at approximately 15° South, 15° West, and with a 30% S-wave velocity reduction. Significant uncertainties and trade-offs do remain to these parameters, but a large ULVZ is needed to explain the data. The location is west of St. Helena and south of Ascension. Helium and neon isotopic systematics observed in samples from this region could point to a less-outgassed mantle component mixed in with the dominant signature of recycled material. These observations could be explained by a contribution from the Large Low Shear Velocity Province (LLSVP). Tungsten isotopic measurements would be needed to understand whether a contribution from the mega-ULVZ is also required at St. Helena or Ascension.

Plain Language Summary

Nearly 3,000 kilometres beneath the Atlantic to the West of the island of St. Helena, on the boundary between Earth's metal core and rocky mantle, we have discovered a new area where seismic waves diffracting along that boundary travel significantly slower than expected. This area is called an ultra-low velocity zone.

In this study, we use seismic waves which propagate along the core-mantle boundary. The waves that interact with the ultra-low velocity zone are scattered and become severely delayed. Using the observations, we have constrained the ultra-low velocity zone to a broadly cylindrical structure, 600 km across, 20 km high and centred at 15° South, 15° West. The material inside is reduced by 30% in seismic shear wave velocity compared to outside. We confirmed this model by computing and comparing synthetic waveforms for a range of different ultra-low velocity zone models. This position sits against a much larger region of low velocity, dubbed the African Large Low Shear-Velocity Province (LLSVP). The observed ultra-low velocity zone could be the base of the upwelling or mantle plume rising through the mantle and causing the hotspots of St. Helena and/or Ascension at the surface.

1 Introduction

The core-mantle boundary (CMB) is both an area of significance in mantle dynamics - being the lower thermal boundary layer in mantle convection - and a region of great lateral heterogeneity as observed by seismology. This heterogeneity is most notable in the two antipodal large low shear-velocity provinces (LLSVPs) extending upwards as far as 1000 km at the highest point (e.g., Cottaar & Lekic, 2016) - one beneath the Pacific and one beneath Africa. Beyond these comparatively well-imaged structures, scattered smaller-scale heterogeneities - tens of kilometres high, and hundreds across - with extreme velocity reductions are found and dubbed Ultra-Low Velocity Zones (ULVZs) (e.g., Yu & Garnero, 2018). A number of ULVZs - including the largest of those modelled in 3D - have been found at or near the base of major mantle plumes, specifically those underlying the Hawaiian (Cottaar & Romanowicz, 2012; Jenkins et al., 2021; Lai et al., 2022; Z. Li et al., 2022; J. Li et al., 2022; Martin et al., 2023a), Icelandic (Yuan & Romanowicz, 2017), Samoan (Thorne et al., 2013; Krier et al., 2021), and Galápagos (Cottaar et al., 2022) hotspots.

While the composition and internal structure of ULVZs remains uncertain, their extreme velocity reductions mean they must have anomalous compositions. One candidate is magnesiowüstite enrichment (e.g., Dobrosavljevic et al., 2019), and another is the presence of partial melt (e.g., Kimura et al., 2017; Dannberg et al., 2021). The consistent association of the well-characterised "mega-ULVZs" - Hawaii, Iceland, Samoa and Galápagos - with isotopic anomalies in the ocean island basalts (e.g., Jackson et al., 2017; Mundl et al., 2017) implies the ULVZs might have either a primordial origin or had significant chemical exchange with the core (Mundl-Petermeier et al., 2020).

Many more ULVZs are mapped beneath the Pacific Ocean, and are potentially associated with the Pacific LLSVP, compared to the region beneath Africa and the Atlantic, which could be associated with the African LLSVP (e.g. compilation in Yu & Garnero, 2018). This difference could be due to less optimal earthquake-station geometries targeting the core-mantle boundary beneath the Atlantic and Africa. Up to now, there has been one mega-ULVZ mapped at the northern edge of the African LLSVP beneath Iceland (Yuan & Romanowicz, 2017). Evidence of presence of ULVZs is found further south and west within and around the edges of the LLSVP (Helmberger et al., 2000; Ni & Helmberger, 2001a, 2001b; Wen, 2000; Thorne et al., 2021). There are a number of volcanic hotspots across the Southern Atlantic that are thought to be underlain by whole mantle plumes (S. W. French & Romanowicz, 2015; Marignier et al., 2020). The question remains if these could also linked to the presence of mega-ULVZs at or near their base.

Here we target a large swath of the CMB beneath the Atlantic around the equator using shear diffracted (S_{diff}) body-waves. Diffracted waves along the core-mantle boundary are slowed significantly within a ULVZ and refracted at its edges, leading to a delayed secondary arrival or postcursor (Fig. 1). The postcursory energy refracted by the ULVZ arrives at stations delayed and from a different angle. We find evidence of postcursors caused by a previously unmapped ULVZ at the CMB to the west of St. Helena. We use data from four principal earthquakes with varied azimuthal sensitivity to model the ULVZ in further detail. We compare with synthetic seismograms produced for a range of 3D cylindrical ULVZ models, to constrain its rough position, height, width, and velocity reduction.

2 Methods and Data

2.1 Data Catalogue and Assessment

To distinguish S_{diff} postcursors from depth phases requires dense station coverage to observe the postcursor move-out as it varies with azimuth. Additionally, the ULVZ needs to be sampled from different azimuthal directions to be accurately located. As such,

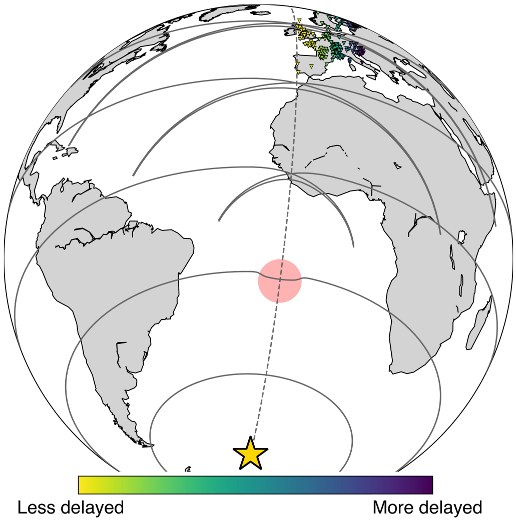

Figure 1. A series of wavefronts passing through a model ULVZ. Geometry is for a ULVZ near St. Helena and an earthquake at the South Sandwich Islands recorded at stations across Europe. The arcuate shape of the postcursor means it will arrive later at stations further from the event-ULVZ axis (dashed line).

we considered three principal geometries which sample beneath the Atlantic around the equator: from Prince Edward Island to the East Coast of North America; from the South Sandwich islands to Western Europe; and from Peru to East Africa. We analysed earthquakes over magnitude 5.7 at the correct distance range (95-135°) to sample the CMB. All 27 earthquakes considered are listed in the Supporting Information. As the SV energy of S_{diff} converts readily to P-waves in the outer core, and therefore attenuates strongly along the CMB leg of the ray-path, we use the SH energy on the transverse component.

While prior studies of S_{diff} typically involved visual assessment of data for quality control (e.g., Cottaar et al., 2022), here we implement an automated and reproducible approach. Our algorithm exploits the fact that the postcursors move-out with time as a function of azimuth with respect to the main phase. Thus, the postcursor will stack coherently in local azimuth bins, but not across wide azimuth bins. Our algorithm follows the following steps for each event:

1. Data is filtered between 10 and 35 s.
2. Data is windowed between -20 and 100 seconds before and after the predicted S_{diff} phase arrival.
3. We create bins of waveforms for each degree azimuth, and create linear stacks within each bin. This is referred to as the 'local' stack.
4. A linear stack of all waveforms in a densely sampled area is created using all waveforms that correlate strongly (>0.8) with their 'local' stack. We refer to this as the 'global' stack.
5. To ensure a good signal-to-noise ratio, waveforms with less than .2 correlation to the global stack are rejected.
6. Each remaining waveform that correlates more with the global stack than the local stack is rejected, unless the correlation coefficient with either the local or the global stack exceeds 0.8.

The exception to the final rule is to reduce the loss of high-quality traces without a postcursor, which might correlate well to the global stack, and thus the loss of 'null' results. Visual examples of the waveforms we accept and reject are included in the Supporting Information. Our algorithm offers advantages in ease-of-use and scalability, and requires minimal tuning. Advantages over "by-eye" assessment are in reproducibility, robustness, and speed.

After quality control, we select four comparatively high quality events covering the range of geometries shown in Fig. 2 to model in further detail.

2.2 Synthetic Modelling

We produce synthetic seismograms using sandwiched-CSEM, the "sandwiched" version of the Coupled Spectral Element Method (Capdeville et al., 2003). In this method, a spectral element solution is calculated only for the lowermost 370 km of the mantle, with a normal mode solution used for both the core and the remainder of the mantle and crust. This allows us the implement the 3D structure of interest at the core-mantle boundary, while reducing computational cost such that we can compute synthetics for many models down to 10 s period; prior studies including Yuan and Romanowicz (2017) and Cottaar et al. (2022) have used the same method.

To simplify the model space down to a computationally tractable problem, we assume a cylindrical ULVZ, and attempt to find values for its radius, height, location and shear-wave velocity reduction. As the model space remains too broad for a full grid search of all parameters, we instead iterate by producing synthetic seismograms from a model, visually comparing move-out patterns, and updating the model accordingly to improve the fit.

Our background model within the 3D modelled region for shear wave velocity is SEMUCB-WM1 (S. French & Romanowicz, 2014). This tapers towards the background 1D model in the top 70 km of the SEM mesh. Inside the ULVZ, we reduce V_S according to the model in use. The choice of P-wave velocity and density in the ULVZ have negligible impact on the resultant waveforms; our model scales dV_P equally to dV_S, and density deviation by $-\frac{1}{2}dV_S$, meaning the ULVZ is heavy. We present our best-fitting ULVZ in the main paper and illustrate trade-offs in the Supporting Information.

3 Results

3.1 Dataset and Selected Earthquake Parameters

The four earthquakes we base our model on are outlined in Fig. 2 and Table 1. Events A and B are in the Prince Edward Island region and their S_{diff} waves are recorded across the eastern United States, with the Transportable Array providing excellent coverage with azimuth to identify postcursors. While this geometry gives us dense, high quality observations, it is on its own not sufficient to locate the ULVZ. As such, events C and D - from the South Sandwich Islands to Europe and from Peru to East Africa, respectively - provide useful crossing ray path coverage to help constrain the location, as well as providing independent checks on the success of synthetic models.

Figs. 3 to 6 show real and synthetic data for these events. Waveforms are centred on the predicted S_{diff} arrival time (for PREM, Dziewonski & Anderson, 1981) and filtered between 10 and 30 seconds period. Waveforms are organised by azimuth from their event, rounded to the nearest degree, to make the plots clearer. Interpreted postcursors are highlighted for each event and show a move-out as a function of azimuth.

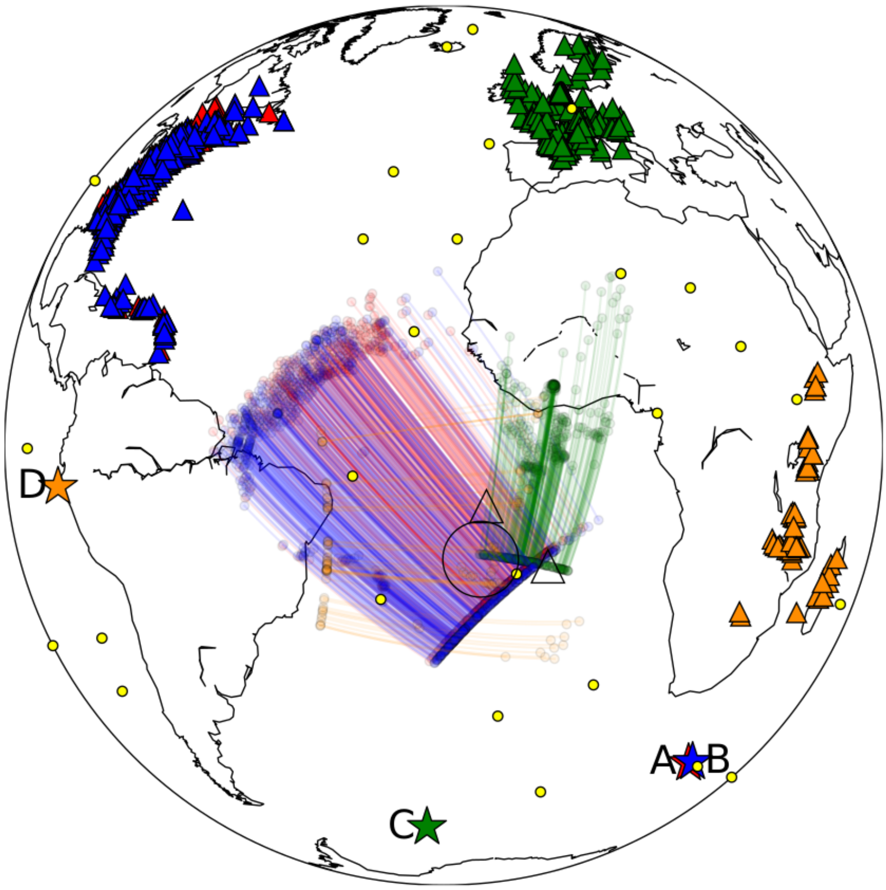

Figure 2. Map showing the coverage on the core-mantle boundary of S_{diff} ray-paths. Stars are earthquake sources, labelled by event and triangles are receivers. Event A- red, event B- blue, event C-green, event D- yellow. Coloured lines between circles show where the great circle ray paths are sensitive to the core-mantle boundary; note that scattered postcursory phases will follow different paths. Our preferred ULVZ model is shown as a circle, centred at 15°S, 15°W, and a radius of 300 km. Major hotspots are shown as yellow circles and the volcanic islands of Ascension and St. Helena are shown as triangles.

ID	Date	Lon. [°E]	Lat. [°N]	M_W	Depth [km]	Location
A	2014/11/17	33.79	-46.27	6.2	17.6	Prince Edward Island
B	2013/07/22	34.93	-45.89	6.3	20.7	Prince Edward Island
C	2021/08/22	-23.60	-60.33	6.7	12.0	South Sandwich Islands
D	2013/08/12	-82.13	-5.52	6.2	12.0	Off Coast of Peru

Table 1. Earthquake source parameters. From the Global Centroid-Moment-Tensor project (Ekström et al., 2012).

All four events occurred between depths of 12 and 21 km, and their depths phases arrive within the wave train for this period band. The interpreted postcursors merge with the main wave train in events A, B, and D, and to a lesser degree in C.

3.2 Preferred Model Parameters

Two sets of synthetic data are also presented in Figs. 3 to 6. One includes 3D velocity variations as in SEMCUCB for the lowermost mantle, and the other includes our best model ULVZ on top of the background model.

The model producing the best-fitting synthetics includes a cylindrical ULVZ centred at 15°S, 15°W with a diameter of 600 km and a height of 20 km. This width on the core-mantle boundary covers almost 10°. Within the ULVZ, V_S is reduced by 30%.

Across all events, the main S_{diff} phases in the data arrive much later than in the synthetics. The S_{diff} phases in the various orientations all travel through the African LLSVP. The delays caused by this anomaly are likely underestimated by our model as - using the sandwiched-CSEM - we can only include a 3D model in the lowermost 300 km of the mantle, while particularly the African LLSVP can extend much higher (Cottaar & Lekic, 2016). To allow for comparison, the highlight for the interpreted postcursor is shifted 5 seconds earlier in the synthetics.

Individual traces are normalised, allowing for comparison for relative amplitudes instead of absolute amplitudes. Generally, the relative amplitude of the postcursor with respect to the main phase is well predicted. The relative delay time between the postcursor and main phase is well fit in events C and D, and slightly large for events A and B.

Our preferred ULVZ demonstrates a cylindrical ULVZ can roughly explain the observed postcursors. This is likely not a unique model within our simplified model space. An exploration of models with varied parameters is included in the supplementary materials to illustrate the potential errors in the model. Changing the location by 4° shows a noticeable shift in the minimum travel time move-out for the postcursors. Larger and wider ULVZs increase the amplitudes and delay times of the S_{diff} postcursors. Delay times are also affected by the choice of velocity reduction. There is a trade-off between size and velocity reduction resulting in comparable delay times for the postcursors.

Waveform results comparing predictions for our preferred model to the observations for two further events are shown in the Supporting Information. One of these complements what we see for event C here. The other shows an example from a new geometry where strong postcursors should be expected, but are not clearly observed. This could be due to the noisy data, but might also indicated there is some unmodelled asymmetry to the model.

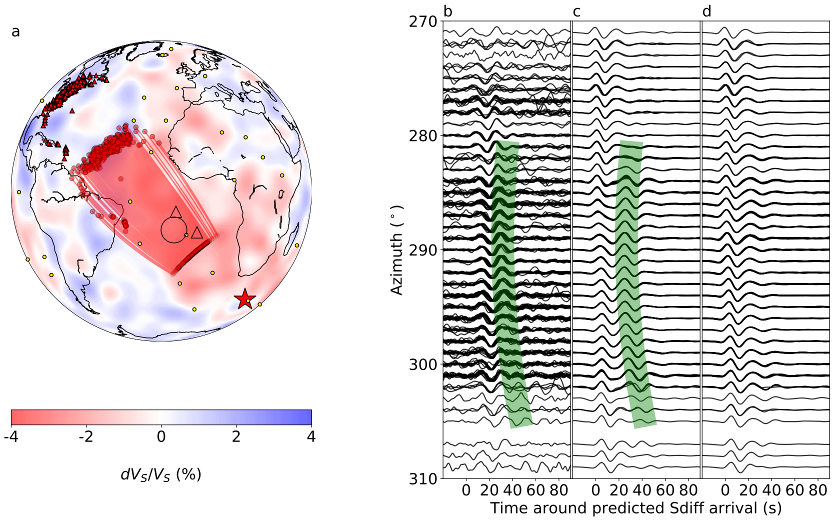

Figure 3. Map and waveforms for event A. a. Map showing ray paths and proposed ULVZ location. Background velocity model is a depth slice through SEMUCB-WM1 (S. French & Romanowicz, 2014) at 2800 km depth. b. Observed data with interpreted postcursors highlighted in green. c. Synthetics including the proposed ULVZ model within SEMUCB-WM1. Same highlight is shown as in b. shifted by -5 seconds (as our S_{diff} waves arrive earlier in the synthetics, see text for discussion). d. Synthetics for SEMUCB-WM1.

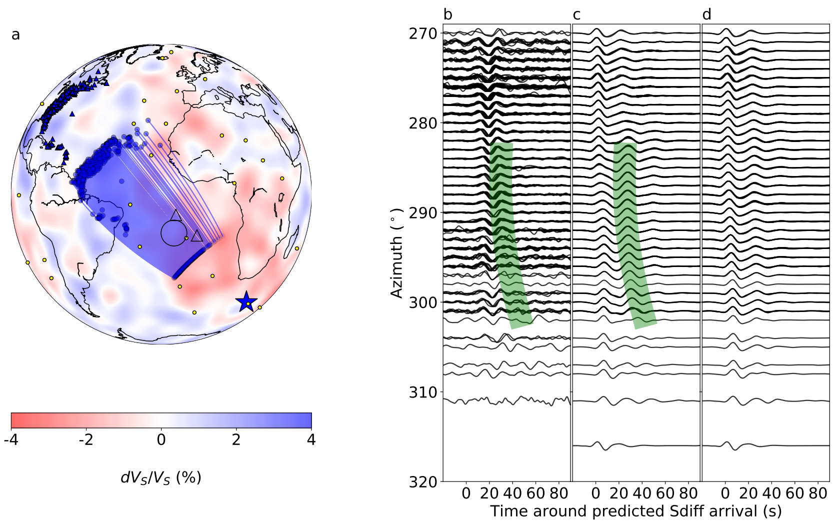

Figure 4. Map and waveforms for event B. a. Map showing ray paths and proposed ULVZ location. Background velocity model is a depth slice through SEMUCB-WM1 at 2800 km depth. b. Observed data with interpreted postcursors highlighted in green. c. Synthetics including the proposed ULVZ model within SEMUCB-WM1. Same highlight is shown as in b. shifted by -5 seconds. d. Synthetics for SEMUCB-WM1.

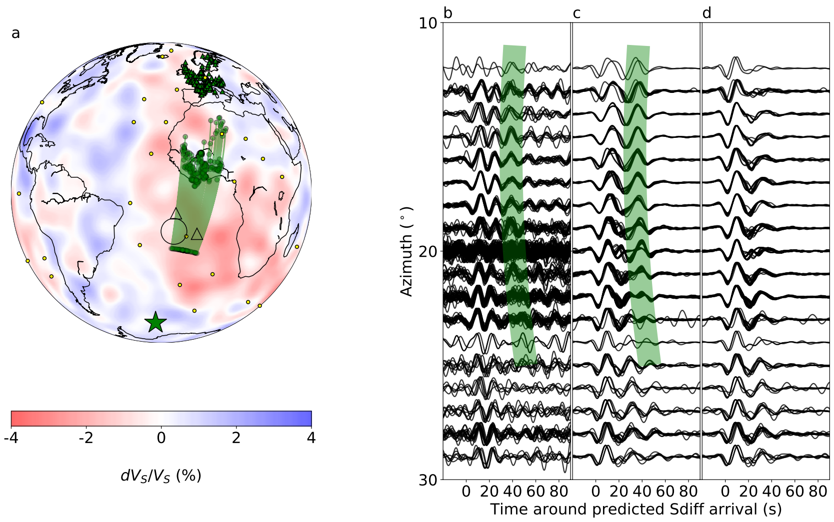

Figure 5. Map and waveforms for event C. a. Map showing ray paths and proposed ULVZ location. Background velocity model is a depth slice through SEMUCB-WM1 at 2800 km depth. b. Observed data with interpreted postcursors highlighted in green. c. Synthetics including the proposed ULVZ model within SEMUCB-WM1. Same highlight is shown as in b. shifted by -5 seconds. d. Synthetics for SEMUCB-WM1.

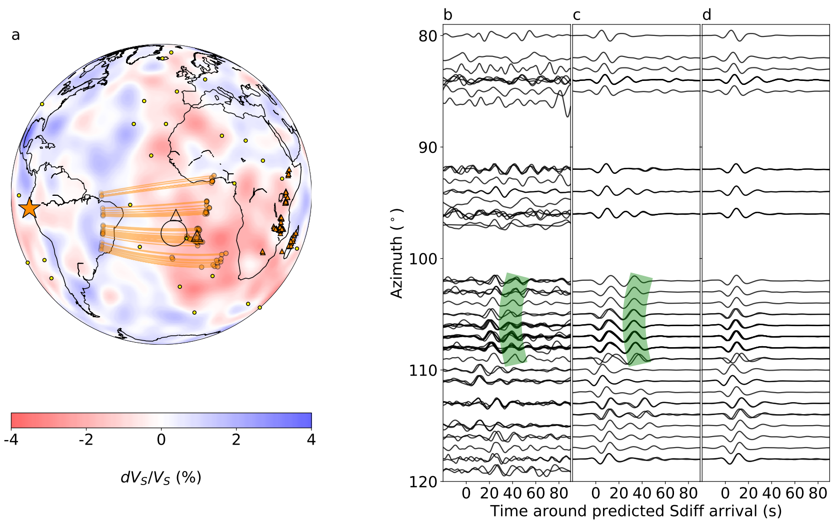

Figure 6. Map and waveforms for event D. a. Map showing ray paths and proposed ULVZ location. Background velocity model is a depth slice through SEMUCB-WM1 at 2800 km depth. b. Observed data with interpreted postcursors highlighted in green. c. Synthetics including the proposed ULVZ model within SEMUCB-WM1. Same highlight is shown as in b. shifted by -5 seconds. d. Synthetics for SEMUCB-WM1.

4 Discussion

4.1 Limitations in parameterisation

Our model does not fit all four events equally well. Likely there are lateral variations and asymmetries in the actual ULVZ that could account for some of the variations, but it is difficult and computationally intensive to assess more parameters in our forward modelling approach. For the Hawaiian ULVZ, the potential of a Bayesian inversion for an elliptical shape has been demonstrated, for which the results showed alignment along the LLSVP boundary (Martin et al., 2023b, 2023a). This approach requires careful picking of the postcursor travel time delays, which is challenging to do for the generally sparser and lower quality data we have here.

While the exact location is uncertain up to several degrees, the good azimuthal coverage does limit where the ULVZ could be. The ULVZ is constrained to lie beneath the vicinity of the St. Helena and Ascension hotspot locations.

4.2 Comparison to Other ULVZs

The discovered 'Atlantic' ULVZ lies on the core-mantle boundary to the west of the St. Helena hotspot and to the south of Ascension. No previous studies with other seismic probes suggest evidence of a ULVZ in this region (see compilation in Yu & Garnero, 2018). Global compilations of SPdKS data have too little coverage in this area to observe a ULVZ (Thorne et al., 2021). Ni and Helmberger (2001a) show some evidence of patchy ULVZ material further to the West. Generally, there have been few studies finding ULVZs beneath the Atlantic.

Our modelled Atlantic ULVZ is of comparable size to "mega-ULVZs" in the literature that have been located near major hotspots (e.g., Cottaar et al., 2022; Jenkins et al., 2021; Yuan & Romanowicz, 2017; Cottaar & Romanowicz, 2012; J. Li et al., 2022; Lai et al., 2022; Krier et al., 2021). All of these are located within LLSVPs, but near their edge. The Atlantic ULVZ is the second ULVZ, after the one beneath Iceland, that can be linked to the African LLSVP.

While we have modelled its geometry as cylindrical to make synthetic modelling tractable, investigations for ScS pre- and postcursors for Hawaii have shown the mega-ULVZ there has varied morphology (Jenkins et al., 2021). Such modelling requires shorter distance event-station geometry, for which the bounce point samples the ULVZ. Applying this to the Atlantic ULVZ would require new networks of land-based and ocean-bottom seismometers. Data for the Hawaiian ULVZ has also shown internal layering (Z. Li et al., 2022), but such analyses would require higher quality data than is presently available.

Our observations do not provide a direct constraint on the density of the ULVZ. However, the estimated aspect ratio of the ULVZ of 600 km wide and 20 km tall means the density contrast must be large (Bower et al., 2011). Such broad-scale features have been recreated in 3D geodynamical models by including 'ultradense' material (M. Li et al., 2017). The observed morphology does not result if ULVZ material is caused purely by partial melting (Dannberg et al., 2021), but partial melting could occur within an already compositionally distinct material.

4.3 Potential links to hotspot locations

Whether (mega-)ULVZs are linked to and play a role in mantle plume dynamics remains speculative. Mega-ULVZs are detected beneath the major hotspots, Hawaii, Iceland, Samoa, and Galápagos, where large buoyancy fluxes are observed (Hoggard et al., 2020) and whole mantle plumes have been imaged (e.g. S. W. French & Romanowicz, 2015). Additionally, basalts from these hotspots exhibit high $^3He/^4He$ isotope ratios, solar-like neon isotopes, and negative deviations in tungsten isotope ratios that have been suggested to reflect a combination of ULVZ and LLSVP signatures (Mundl-Petermeier et al., 2020; Cottaar et al., 2022). However, a recent study also shows that the Marquesas shows high $^3He/^4He$ isotope ratio, but no deviation in tungsten isotope ratios (Herret et al., 2023), even though there is suggested to be a ULVZ at its base (Kim et al., 2020).

St. Helena and Ascension are hotspot locations with a weak buoyancy flux (Hoggard et al., 2020). The shear wave tomographic model of S. W. French and Romanowicz (2015) observes a whole mantle plume beneath St. Helena. Based on this model, Bao et al. (2022) categorise St. Helena as a 'warm', but not a 'hot' plume, and Ascension as a 'cold' plume, suggesting the latter might not have a deep-seated source. However, based on a range of tomographic models, Marignier et al. (2020) conclude a higher possibility of a deep-seated plume beneath Ascension than for St. Helena. The nature of the plumes, if both hotspots are fed by a common plume source, and where the plume(s) interact with the African LLSVP and the core-mantle boundary remains uncertain.

St. Helena is geochemically categorised as a HIMU hotspot ("high μ," where μ is the $^{238}U/^{204}Pb$ ratio of the mantle source). Alpha decay of radioactive ^{238}U with a half-life of 4.47 Ga (Villa et al., 2022) produces ^{206}Pb over time. Basalts from St. Helena and other HIMU ocean islands, such the Cook-Austral Islands and the Canary Islands, exhibit extremely radiogenic Pb isotopic signatures (high ratios of radiogenic ^{206}Pb to non-radiogenic ^{204}Pb) that require evolution of a source with high U/Pb (high μ) for $\sim$1.5 to 2 Gyr timescales (Chauvel et al., 1992; Zindler & Hart, 1986). The HIMU Pb isotopic signature is attributed to ancient recycled oceanic crust in the mantle source, as slab processing during seafloor alteration and dehydration upon subduction generates high U/Pb in the crust (Kelley et al., 2005). Various stable isotope ratios support the interpretation of radiogenic Pb isotopes as indicative of recycled crust in HIMU mantle sources, including Ba, Li, Tl and Zn isotopes (Bai et al., 2022; Blusztajn et al., 2018; Chan et al., 2009; X.-Y. Zhang et al., 2022), though alternate hypotheses have been put forth (see review in Weis et al., 2023). Nearly all hotspots, including St. Helena, have also been suggested to be basalt-enriched based on the presence of the seismically observable "X discontinuity" around 300 km depth (Kemp et al., 2019; Pugh et al., 2021).

Ancient dehydrated recycled oceanic crust should have extremely radiogenic He isotopes. Crust is thoroughly degassed of its original He, and ^4He is produced by alpha decay of U and Th while ^3He is not produced in significant quantities over time. After 2 billion years of residence in the mantle, recycled crust is expected to develop a $^3He/^4He$ of $\sim$0.01 Ra (where Ra is the atmospheric ratio of 1.39×10^{-6}) (Barfod et al., 1999). However, HIMU He isotope ratios range from $\sim$4-7 Ra (Barfod et al., 1999; Graham et al., 1992; Day & Hilton, 2011; Hanyu et al., 2011, 2014; Hanyu & Kaneoka, 1997; Parai et al., 2009; Sandoval-Velasquez et al., 2023; X. J. Zhang et al., 2024). The observation that HIMU $^3He/^4He$ ratios (including in samples from St. Helena; Graham et al., 1992; Hanyu et al., 2011) are higher than expected for pure recycled oceanic crust is best explained by mixing between recycled crust and a component with higher $^3He/^4He$. While HIMU He isotopes could be consistent with recycled crust mixing with the mantle source of mid-ocean ridge basalts (MORBs, $\sim$7-9 Ra), HIMU Ne isotopic data from the Cook-Australs (Parai et al., 2009; X. J. Zhang et al., 2024), Canary Islands (Sandoval-Velasquez et al., 2023) and one Ne measurement from St. Helena (Moreira et al., 2003) are more primitive in character (i.e., come from a less-outgassed reservoir) than the MORB mantle. He-Ne isotope systematics require that HIMU plumes contain a mixture of recycled crust and a high $^3He/^4He$ component similar to that observed in Hawaii, Iceland, Galapagos, or Samoa (X. J. Zhang et al., 2024).

Ascension is characterized by moderate HIMU Pb and He isotopic signatures, and has been suggested to sample the same source as St. Helena (Ammon et al., 2009). Ne isotopes measured in basalts from Mid-Atlantic Ridge off-axis seamounts near Ascension are similar to the other HIMU Ne observations and require sampling of a component that is less outgassed than the depleted upper mantle (Stroncik et al., 2007). This could potentially indicate sampling of a deep reservoir, although some debate remains if the mantle plume feeds into this area (Stroncik & Niedermann, 2016).

While further Ne isotopic data from St. Helena are desirable, the geochemical model of mixing between recycled crust and a less-outgassed mantle component could be consistent with a contribution from a reservoir at the base of the mantle. The relatively low St. Helena and Ascension $^3He/^4He$ ratios may reflect masking of a high $^3He/^4He$ signature by mixing with recycled crust rich in ^4He, while the impact of recycled crust on the Ne isotopic composition of the mixed plume would be muted due to the very low $^{21}Ne/^4He$ production ratio ($\sim$4.5 x 10^{-8}; Yatsevich & Honda, 1997). The question remains then whether the LLSVP or the mega-ULVZ is the source of the less-outgassed, high $^3He/^4He$ and primitive Ne isotopic compositions. The anomalous tungsten signatures could be explained by a primordial or core-derived signature that is more easily attributed to the more iron-rich mega-ULVZs (Mundl-Petermeier et al., 2020; Cottaar et al., 2022). Tungsten isotopic data for St. Helena or Ascension would enable further testing of the hypothesis that anomalous tungsten isotopic signatures are found at hotspots associated with mega-ULVZs.

5 Conclusions

We discovered an ultra-low velocity zone beneath the Atlantic Ocean through S_{diff} postcursors and have developed an approximate model which reproduces the S_{diff} postcursors seen in real data, as well as the directionality of scattered energy. From comparison of real and synthetic waveforms, beamforming, and frequency analysis, we constrain our model to a cylinder 600 km across, 20 km high, and with 30% V_S reduction, at 15 ± 3°S, 15 ± 3°W. The intensity of postcursory and scattered energy may imply that the true ULVZ is non-axisymmetric. Unlike other ocean islands above modelled mega-ULVZs such as Hawaii, Iceland, Samoa and Galápagos, St. Helena and Ascension's geochemical signatures reflect sampling of a HIMU reservoir. A geochemical signature from the LLSVP and/or ULVZ could be present, but would need further characterisation.

Open Research Section

The facilities of IRIS Data Services, and specifically the IRIS Data Management Center, were used for access to waveforms, related metadata, and/or derived products used in this study. IRIS Data Services are funded through the Seismological Facilities for the Advancement of Geoscience (SAGE) Award of the National Science Foundation under Cooperative Support Agreement EAR-1851048.

Specific arrays used for events A and B were TA (https://doi.org/10.7914/SN/TA), X8 (https://doi.org/10.7914/SN/X8_2012), LD (https://doi.org/10.7914/SN/LD), US (https://doi.org/10.7914/SN/US), NE (https://doi.org/10.7914/SN/NE), CN (https://doi.org/10.7914/SN/CN), N4 (https://doi.org/10.7914/SN/N4), CU (https://doi.org/10.7914/SN/CU), 7A (https://doi.org/10.7914/SN/7A_2013), G (https://doi.org/10.18715/GEOSCOPE.G), ZL (https://doi.org/10.7914/SN/ZL_2011), IU (https://doi.org/10.7914/SN/IU), Y6 (Imperial College London, 2013), WI (https://doi.org/10.18715/antilles.WI), ZC (https://doi.org/10.7914/SN/ZC_2013), PO (Geological Survey of Canada, 2000), XO (https://doi.org/10.7914/SN/XO_2011), PE (https://doi.org/10.7914/SN/PE), CO (https://doi.org/10.7914/SN/CO), GL (https://doi.org/10.18715/guadeloupe.gl), TR (EUniversity of the West Indies, 1965), YO (https://doi.org/10.7914/SN/YO_2014), PR (https://doi.org/10.7914/SN/PR), MQ (https://doi.org/10.18715/martinique.mq), WU (Nanometrics Seismological Instruments, 1991), XQ (https://doi.org/10.7914/SN/XQ_2012), Z9 (https://doi.org/10.7914/SN/Z9_2010), ZU (University of Southampton, 2013), II (https://doi.org/10.7914/SN/II), ET (University of Memphis, 1982), and DR (https://doi.org/10.7914/SN/DR).

Arrays used for event C were NL (https://doi.org/10.21944/e970fd34-23b9-3411-b366-e4f72877d2c5), GB (British Geological Survey, 1970), CZ (https://doi.org/10.7914/SN/CZ), SL (https://doi.org/10.7914/SN/SL), UP (https://doi.org/10.18159/SNSN), FR (https://doi.org/10.15778/RESIF.FR), CH (https://doi.org/10.12686/sed/networks/ch), HE (https://doi.org/10.14470/UR044600), RD (https://doi.org/10.15778/RESIF.RD), LX (https://doi.org/10.7914/SN/LX), OX (https://doi.org/10.7914/SN/OX), OE (https://doi.org/10.7914/SN/OE), MN (https://doi.org/10.13127/SD/fBBBtDtd6q), HU (https://doi.org/10.14470/UH028726), IM, DK (GEUS Geological Survey of Denmark and Greenland, 1976), IU (https://doi.org/10.7914/SN/IU), GR (https://doi.org/10.25928/mbx6-hr74), SK (https://doi.org/10.14470/FX099882), CA (https://doi.org/10.7914/SN/CA), G (https://doi.org/10.18715/GEOSCOPE.G), II (https://doi.org/10.7914/SN/II), EE (Geological Survey of Estonia, 1998), SS (https://doi.org/10.7914/SN/SS), MT (https://doi.org/10.15778/RESIF.MT), FN (Sodankyla Geophysical Observatory / University of Oulu, 2005), LC (https://doi.org/10.7914/SN/LC), GE (https://doi.org/10.14470/TR560404), BE (https://doi.org/10.7914/SN/BE), KO (https://doi.org/10.7914/SN/KO), Z3 (https://doi.org/10.12686/alparray/z3_2015), CL (https://doi.org/10.15778/RESIF.CL), HT (https://doi.org/10.7914/SN/HT), HL (https://doi.org/10.7914/SN/HL), HC (https://doi.org/10.7914/SN/HC), WM (https://doi.org/10.14470/JZ581150), HP (https://doi.org/10.7914/SN/HP), YW (https://doi.org/10.15778/RESIF.YW2017), RO (https://doi.org/10.7914/SN/RO), HA (https://doi.org/10.7914/SN/HA), MP (https://doi.org/10.7914/SN/MP), and TU (https://doi.org/10.7914/SN/TU).

Arrays used for event D were XK (https://doi.org/10.7914/SN/XK_2012), IU (https://doi.org/10.7914/SN/IU), NJ (https://doi.org/10.7914/SN/NJ), YQ (https://doi.org/10.7914/SN/YQ_2013), XM (https://doi.org/10.7914/SN/XM_2012), XV (https://doi.org/10.7914/SN/XV_2011), GE (https://doi.org/10.14470/TR560404), 1C (https://doi.org/10.7914/SN/1C_2011), AF (https://doi.org/10.7914/SN/AF), XJ (https://doi.org/10.7914/SN/XJ_2013), and YV (https://doi.org/10.15778/RESIF.YV2011).

Acknowledgments

With thanks to Stuart Russell, Florian Millet and Stephen Pugh for help with debugging and general advice.

This project has received funding from the European Research Council (ERC) under the European Union's Horizon 2020 research and innovation programme (grant agreement No. 804071 -ZoomDeep). RP was supported by National Science Foundation Grant EAR 2145663.

This work was performed using resources provided by the Cambridge Service for Data Driven Discovery (CSD3) operated by the University of Cambridge Research Computing Service (www.csd3.cam.ac.uk), provided by Dell EMC and Intel using Tier-2 funding from the Engineering and Physical Sciences Research Council (capital grant EP/T022159/1), and DiRAC funding from the Science and Technology Facilities Council (www.dirac.ac.uk).

References

Ammon, K., Dunai, T., Stuart, F., Meriaux, A.-S., & Gayer, E. (2009). Cosmogenic 3He exposure ages and geochemistry of basalts from Ascension Island, Atlantic Ocean. *Quaternary Geochronology*, *4*(6), 525–532. doi: https://doi.org/10.1016/j.quageo.2009.09.003

Bai, R., Jackson, M. G., Huang, F., Moynier, F., Devos, G., Halldórsson, S. A., … Nan, X. (2022). Barium isotopes in ocean island basalts as tracers of mantle processes. *Geochimica et Cosmochimica Acta*, *336*, 436-447. doi: https://doi.org/10.1016/j.gca.2022.08.023

Bao, X., Lithgow-Bertelloni, C. R., Jackson, M. G., & Romanowicz, B. (2022). On the relative temperatures of Earth's volcanic hotspots and mid-ocean ridges. *Science*, *375*(6576), 57-61. doi: 10.1126/science.abj8944

Barfod, D. N., Ballentine, C. J., Halliday, A. N., & Fitton, J. G. (1999). Noble gases in the cameroon line and the He, Ne, and Ar isotopic compositions of high (HIMU) mantle. *Journal of Geophysical Research: Solid Earth*, *104*(B12), 29509-29527. doi: https://doi.org/10.1029/1999JB900280

Blusztajn, J., Nielsen, S. G., Marschall, H. R., Shu, Y., Ostrander, C. M., & Hanyu, T. (2018). Thallium isotope systematics in volcanic rocks from St. Helena–constraints on the origin of the HIMU reservoir. *Chemical Geology*, *476*, 292–301. doi: https://doi.org/10.1016/j.chemgeo.2017.11.025

Bower, D. J., Wicks, J. K., Gurnis, M., & Jackson, J. M. (2011). A geodynamic and mineral physics model of a solid-state ultralow-velocity zone. *Earth and Planetary Science Letters*, *303*(3-4), 193–202. doi: https://doi.org/10.1016/j.epsl.2010.12.035

Capdeville, Y., Chaljub, E., & Montagner, J. P. (2003). Coupling the spectral element method with a modal solution for elastic wave propagation in global earth models. *Geophysical Journal International*, *152*(1), 34–67. doi: https://doi.org/10.1046/j.1365-246X.2003.01808.x

Chan, L.-H., Lassiter, J. C., Hauri, E. H., Hart, S. R., & Blusztajn, J. (2009). Lithium isotope systematics of lavas from the Cook–Austral islands: constraints on the origin of HIMU mantle. *Earth and Planetary Science Letters*, *277*(3-4), 433-442. doi: https://doi.org/10.1016/j.epsl.2008.11.009

Chauvel, C., Hofmann, A. W., & Vidal, P. (1992). HIMU-EM: c connection. *Earth and Planetary Science Letters*, *110*(1-4), 99-119. doi: https://doi.org/10.1016/0012-821X(92)90042-T

Cottaar, S., & Lekic, V. (2016, 08). Morphology of seismically slow lower-mantle structures. *Geophysical Journal International*, *207*(2), 1122-1136. doi: 10.1093/gji/ggw324

Cottaar, S., Martin, C., Li, Z., & Parai, R. (2022, Oct.). The root to the galápagos mantle plume on the core-mantle boundary. *Seismica*, *1*(1). Retrieved from `https://seismica.library.mcgill.ca/article/view/197` doi: 10.26443/seismica.v1i1.197

Cottaar, S., & Romanowicz, B. (2012). An unsually large ULVZ at the base of the mantle near Hawaii. *Earth and Planetary Science Letters*, *355*, 213–222. doi: https://doi.org/10.1016/j.epsl.2012.09.005

Dannberg, J., Myhill, R., Gassmöller, R., & Cottaar, S. (2021). The morphology, evolution and seismic visibility of partial melt at the core–mantle boundary: implications for ULVZs. *Geophysical Journal International*, *227*(2), 1028–1059. doi: https://doi.org/10.1093/gji/ggab242

Day, J. M., & Hilton, D. R. (2011). Origin of 3He/4He ratios in HIMU-type basalts constrained from Canary Island lavas. *Earth and Planetary Science Letters*, *305*(1-2), 226-234. doi: https://doi.org/10.1016/j.epsl.2011.03.006

Dobrosavljevic, V. V., Sturhahn, W., & Jackson, J. M. (2019). Evaluating the role of iron-rich (Mg, Fe) O in ultralow velocity zones. *Minerals*, *9*(12), 762. doi: https://doi.org/10.3390/min9120762

Dziewonski, A. M., & Anderson, D. L. (1981). Preliminary reference Earth model. *Physics of the earth and planetary interiors*, *25*(4), 297–356. doi: https://doi.org/10.1016/0031-9201(81)90046-7

Ekström, G., Nettles, M., & Dziewoński, A. (2012). The global CMT project 2004–2010: Centroid-moment tensors for 13,017 earthquakes. *Physics of the Earth and Planetary Interiors*, *200-201*, 1-9. doi: https://doi.org/10.1016/j.pepi.2012.04.002

French, S., & Romanowicz, B. A. (2014). Whole-mantle radially anisotropic shear velocity structure from spectral-element waveform tomography. *Geophysical Journal International*, *199*(3), 1303–1327. doi: https://doi.org/10.1093/gji/ggu334

French, S. W., & Romanowicz, B. (2015, September). Broad plumes rooted at the base of the Earth's mantle beneath major hotspots. *Nature*, *525*(7567), 95–99. doi: 10.1038/nature14876

Graham, D. W., Humphris, S. E., Jenkins, W. J., & Kurz, M. D. (1992). Helium isotope geochemistry of some volcanic rocks from saint helena. *Earth and Planetary Science Letters*, *110*(1-4), 121–131. doi: https://doi.org/10.1016/0012-821X(92)90043-U

Hanyu, T., & Kaneoka, I. (1997). The uniform and low 3He/4He ratios of HIMU basalts as evidence for their origin as recycled materials. *Nature*, *390*(6657), 273-276. doi: https://doi.org/10.1038/36835

Hanyu, T., Kawabata, H., Tatsumi, Y., Kimura, J.-I., Hyodo, H., Sato, K., … others (2014). Isotope evolution in the HIMU reservoir beneath St. Helena: Implications for the mantle recycling of U and Th. *Geochimica et Cosmochimica*

Acta, *143*, 232–252. doi: https://doi.org/10.1016/j.gca.2014.03.016

Hanyu, T., Tatsumi, Y., & Kimura, J.-I. (2011). Constraints on the origin of the HIMU reservoir from He–Ne–Ar isotope systematics. *Earth and Planetary Science Letters*, *307*(3-4), 377–386. doi: https://doi.org/10.1016/j.epsl.2011.05.012

Helmberger, D., Ni, S., Wen, L., & Ritsema, J. (2000). Seismic evidence for ultralow-velocity zones beneath Africa and eastern Atlantic. *Journal of Geophysical Research: Solid Earth*, *105*(B10), 23865-23878. doi: https://doi.org/10.1029/2000JB900143

Herret, M.-T., Peters, B., Kim, D., Castillo, P., & Mundl-Petermeier, A. (2023). Decoupling of short-lived radiogenic and helium isotopes in the Marquesas hotspot. *Chemical Geology*, *640*, 121727. doi: https://doi.org/10.1016/j.chemgeo.2023.121727

Hoggard, M. J., Parnell-Turner, R., & White, N. (2020). Hotspots and mantle plumes revisited: Towards reconciling the mantle heat transfer discrepancy. *Earth and Planetary Science Letters*, *542*, 116317. doi: https://doi.org/10.1016/j.epsl.2020.116317

Jackson, M. G., Konter, J. G., & Becker, T. (2017, February). Primordial helium entrained by the hottest mantle plumes. *Nature*, *542*(7641), 340–343. doi: 10.1038/nature21023

Jenkins, J., Mousavi, S., Li, Z., & Cottaar, S. (2021). A high-resolution map of Hawaiian ULVZ morphology from ScS phases. *Earth and Planetary Science Letters*, *563*, 116885. doi: https://doi.org/10.1016/j.epsl.2021.116885

Kelley, K. A., Plank, T., Farr, L., Ludden, J., & Staudigel, H. (2005). Subduction cycling of U, Th, and Pb. *Earth and Planetary Science Letters*, *234*(3-4), 369-383. doi: https://doi.org/10.1016/j.epsl.2005.03.005

Kemp, M., Jenkins, J., Maclennan, J., & Cottaar, S. (2019). X-discontinuity and transition zone structure beneath Hawaii suggests a heterogeneous plume. *Earth and Planetary Science Letters*, *527*, 115781. doi: https://doi.org/10.1016/j.epsl.2019.115781

Kim, D., Lekić, V., Ménard, B., Baron, D., & Taghizadeh-Popp, M. (2020). Sequencing seismograms: A panoptic view of scattering in the core-mantle boundary region. *Science*, *368*(6496), 1223–1228. doi: 10.1126/science.aba8972

Kimura, T., Ohfuji, H., Nishi, M., & Irifune, T. (2017). Melting temperatures of MgO under high pressure by micro-texture analysis. *Nature communications*, *8*(1), 1–7. doi: https://doi.org/10.1038/ncomms15735

Krier, J., Thorne, M. S., Leng, K., & Nissen-Meyer, T. (2021). A compositional component to the Samoa ultralow-velocity zone revealed through 2-and 3-D waveform modeling of SKS and SKKS differential travel-times and amplitudes. *Journal of Geophysical Research: Solid Earth*, *126*(7), e2021JB021897. doi: https://doi.org/10.1029/2021JB021897

Lai, V. H., Helmberger, D. V., Dobrosavljevic, V. V., Wu, W., Sun, D., Jackson, J. M., & Gurnis, M. (2022). Strong ULVZ and slab interaction at the northeastern edge of the Pacific LLSVP favors plume generation. *Geochemistry, Geophysics, Geosystems*, *23*(2), e2021GC010020. doi: https://doi.org/10.1029/2021GC010020

Li, J., Sun, D., & Bower, D. J. (2022). Slab control on the mega-sized North Pacific ultra-low velocity zone. *Nature communications*, *13*(1), 1–11. doi: https://doi.org/10.1038/s41467-022-28708-8

Li, M., McNamara, A. K., Garnero, E. J., & Yu, S. (2017). Compositionally-distinct ultra-low velocity zones on Earth's core-mantle boundary. *Nature Communications*, *8*(1). doi: 10.1038/s41467-017-00219-x

Li, Z., Leng, K., Jenkins, J., & Cottaar, S. (2022). Kilometer-scale structure on the core–mantle boundary near Hawaii. *Nature communications*, *13*(1), 1–8. doi:

https://doi.org/10.1038/s41467-022-30502-5

Marignier, A., Ferreira, A. M. G., & Kitching, T. (2020). The probability of mantle plumes in global tomographic models. *Geochemistry, Geophysics, Geosystems*, *21*(9), e2020GC009276. (e2020GC009276 10.1029/2020GC009276) doi: https://doi.org/10.1029/2020GC009276

Martin, C., Bodin, T., & Cottaar, S. (2023a). Mapping structures on the core–mantle boundary using Sdiff postcursors: Part II. application to the Hawaiian ULVZ. *Geophysical Journal International*, *235*(3), 2399–2409. doi: https://doi.org/10.1093/gji/ggad345

Martin, C., Bodin, T., & Cottaar, S. (2023b). Mapping structures on the core–mantle boundary using Sdiff postcursors: Part I. Method and validation. *Geophysical Journal International*, *235*(3), 2385–2398. doi: https://doi.org/10.1093/gji/ggad340

Moreira, M., Doucet, S., Madureira, P., Lecomte, A., & Allegre, C. (2003). He-Ne systematics in OIB and the nature of the source of mantle plumes [Conference Proceedings]. In *Agu fall meeting abstracts* (p. V32A-1007). doi: https://doi.org/10.1016/j.jvolgeores.2023.107928

Mundl, A., Touboul, M., Jackson, M. G., Day, J. M., Kurz, M. D., Lekic, V., . . . Walker, R. J. (2017). Tungsten-182 heterogeneity in modern ocean island basalts. *Science*, *356*(6333), 66–69. doi: https://doi.org/10.1126/science.aal4179

Mundl-Petermeier, A., Walker, R., Fischer, R., Lekic, V., Jackson, M., & Kurz, M. (2020). Anomalous 182W in high 3He/4He ocean island basalts: Fingerprints of Earth's core? *Geochimica et Cosmochimica Acta*, *271*, 194–211. doi: https://doi.org/10.1016/j.gca.2019.12.020

Ni, S., & Helmberger, D. V. (2001a). Horizontal transition from fast to slow structures at the core–mantle boundary; South Atlantic. *Earth and Planetary Science Letters*, *187*(3), 301-310. doi: https://doi.org/10.1016/S0012-821X(01)00273-4

Ni, S., & Helmberger, D. V. (2001b). Probing an ultra-low velocity zone at the core mantle boundary with P and S waves. *Geophysical Research Letters*, *28*(12), 2345-2348. doi: https://doi.org/10.1029/2000GL012766

Parai, R., Mukhopadhyay, S., & Lassiter, J. C. (2009). New constraints on the HIMU mantle from neon and helium isotopic compositions of basalts from the cook-austral islands. *Earth and Planetary Science Letters*, *277*(1-2), 253-261. (Times Cited: 1) doi: 10.1016/j.epsl.2008.10.014

Pugh, S., Jenkins, J., Boyce, A., & Cottaar, S. (2021). Global receiver function observations of the X-discontinuity reveal recycled basalt beneath hotspots. *Earth and Planetary Science Letters*, *561*, 116813. doi: https://doi.org/10.1016/j.epsl.2021.116813

Sandoval-Velasquez, A., Rizzo, A., Casetta, F., Ntaflos, T., Aiuppa, A., Alonso, M., . . . Zanon, V. (2023). The noble gas signature of the 2021 Tajogaite eruption La Palma, Canary Islands. *Journal of Volcanology and Geothermal Research*, *443*, 107928. doi: https://doi.org/10.1016/j.jvolgeores.2023.107928

Stroncik, N. A., & Niedermann, S. (2016). He, Ne and Ar isotope signatures of mid-ocean ridge basalts and their implications for upper mantle structure: A case study from the Mid-Atlantic Ridge at 4–12°S. *Geochimica et Cosmochimica Acta*, *183*, 94-105. doi: https://doi.org/10.1016/j.gca.2016.04.002

Stroncik, N. A., Niedermann, S., & Haase, K. M. (2007). Neon and helium isotopes as tracers of mantle reservoirs and mantle dynamics [Journal Article]. *Earth and Planetary Science Letters*, *258*(1), 334-344. Retrieved from `https://www.sciencedirect.com/science/article/pii/S0012821X07002130` doi: https://doi.org/10.1016/j.epsl.2007.03.046

Thorne, M. S., Garnero, E. J., Jahnke, G., Igel, H., & McNamara, A. K. (2013). Mega ultra low velocity zone and mantle flow. *Earth and Planetary Science*

Letters, *364*, 59–67. doi: https://doi.org/10.1016/j.epsl.2012.12.034

Thorne, M. S., Leng, K., Pachhai, S., Rost, S., Wicks, J., & Nissen-Meyer, T. (2021). The most parsimonious ultralow-velocity zone distribution from highly anomalous SPdKS waveforms. *Geochemistry, Geophysics, Geosystems*, *22*(1), e2020GC009467. (e2020GC009467 2020GC009467) doi: https://doi.org/10.1029/2020GC009467

Villa, I. M., Holden, N. E., Possolo, A., Ickert, R. B., Hibbert, D. B., Renne, P. R., . . . De Bievre, P. (2022). IUGS–IUPAC recommendations and status reports on the half-lives of 87Rb, 146Sm, 147Sm, 234U, 235U, and 238U (IUPAC Technical Report) [Journal Article]. *Pure and applied chemistry*, *94*(9), 1085-1092. doi: https://doi.org/10.1515/pac-2021-1202

Weis, D., Harpp, K. S., Harrison, L. N., Boyet, M., Chauvel, C., Farnetani, C. G., . . . Shahar, A. (2023). Earth's mantle composition revealed by mantle plumes. *Nature Reviews Earth Environment*, 1-22. doi: https://doi.org/10.1029/97JB00395

Wen, L. (2000). Intense seismic scattering near the Earth's core-mantle boundary beneath the comoros hotspot. *Geophysical Research Letters*, *27*(22), 3627-3630. doi: https://doi.org/10.1029/2000GL011831

Yatsevich, I., & Honda, M. (1997). Production of nucleogenic neon in the Earth from natural radioactive decay. *Journal of Geophysical Research: Solid Earth*, *102*(B5), 10291-10298. doi: https://doi.org/10.1029/97JB00395

Yu, S., & Garnero, E. J. (2018). Ultralow Velocity Zone locations: A global assessment. *Geochemistry, Geophysics, Geosystems*, *19*(2), 396-414. doi: https://doi.org/10.1002/2017GC007281

Yuan, K., & Romanowicz, B. (2017). Seismic evidence for partial melting at the root of major hot spot plumes. *Science*, *357*(6349), 393–397. doi: https://doi.org/10.1126/science.aan0760

Zhang, X. J., Parai, R., & Lassiter, J. C. (2024). Primordial and recycled noble gases in the Cook-Austral HIMU mantle: Insights into the onset of volatile subduction. *Earth and Planetary Science Letters*, *629*, 118591. doi: https://doi.org/10.1016/j.epsl.2024.118591

Zhang, X.-Y., Chen, L.-H., Wang, X.-J., Hanyu, T., Hofmann, A. W., Komiya, T., . . . Gou, W.-X. (2022). Zinc isotopic evidence for recycled carbonate in the deep mantle. *Nature Communications*, *13*(1), 6085. doi: https://doi.org/10.1038/s41467-022-33789-6

Zindler, A., & Hart, S. (1986). Chemical geodynamics. *Annual Review of Earth and Planetary Sciences*, *14*, 493-571. doi: https://doi.org/10.1146/annurev.ea.14.050186.002425